Chapter 4

Enhancing Damping of Low-Frequency Oscillations in Power Networks through Energy Storage System-Based Controller

4.1 Introduction

Mitigating inter-area Low-Frequency Oscillations (LFOs) is a significant concern in multi-machine power systems due to their adverse effects on system stability. These oscillations are intricately linked with power oscillations. So, appropriate power modulation through the Battery Energy Storage System (BESS) can be an effective strategy for preserving system stability. In this chapter, the maximal of all minimal residue indices under variations in power system operating conditions is utilized as the index for identifying the location for installation of the BESS, the damping control loop, and the feedback signal. A fixed-structure H_∞ scheme-based Wide-Area Damping Controller (WADC) is proposed for the BESS, providing sufficient damping of inter-area oscillation modes. A modified IEEE 39-bus system is simulated using a Real-Time Digital Simulator (RTDS) as a test system in this work. The simulation results confirmed that the proposed WADC could effectively damp various inter-area oscillation modes. Furthermore, it offers robust damping performance over contingencies associated with the system's various operating scenarios as well as the uncertainty associated with fixed and variable communication delays in the

feedback signal of WADC and the integration of solar photovoltaic systems. Moreover, a comparative analysis of the proposed WADC is carried out with a BESS-based Wide-Area Power System Stabilizer (WAPSS), which is found to be more effective in mitigating system inter-area oscillations.

4.2 Power system modelling

This study delves into the impact of BESS and BESS-based WADC on the inter-area oscillation modes within a multi-machine power system. The power system comprises essential components such as SGs, exciters, local PSS, transmission networks, and loads. Each SG is represented as a 6^{th}-order sub-transient model equipped with an IEEE type I excitation system and a type I governor. Transmission networks and loads are modelled using Π models and constant impedance, respectively. The forthcoming subsection provides a detailed discussion of BESS modelling.

4.2.1 Battery energy storage system model

The BESS integrated into the power system comprises the battery pack, Power Conditioning System (PCS), filter, and transformer. The PCS is a group of power converters that work together to keep the power and voltage output at the desired levels. The PCS for the BESS consists of a DC-to-DC bidirectional converter for battery charging/discharging control and a Voltage Source Converter (VSC) for power network integration with required power output and voltage. The elaborate block diagram structure of BESS with the associated controller is shown in Fig. 4.1.

4.2.1.1 Battery pack model

The DC-to-DC converter connects the battery cells in the battery pack module in series and parallel to produce the desired power and voltage. The battery is represented as a controlled DC source in series with an internal resistance R_b based on the generic model [84].

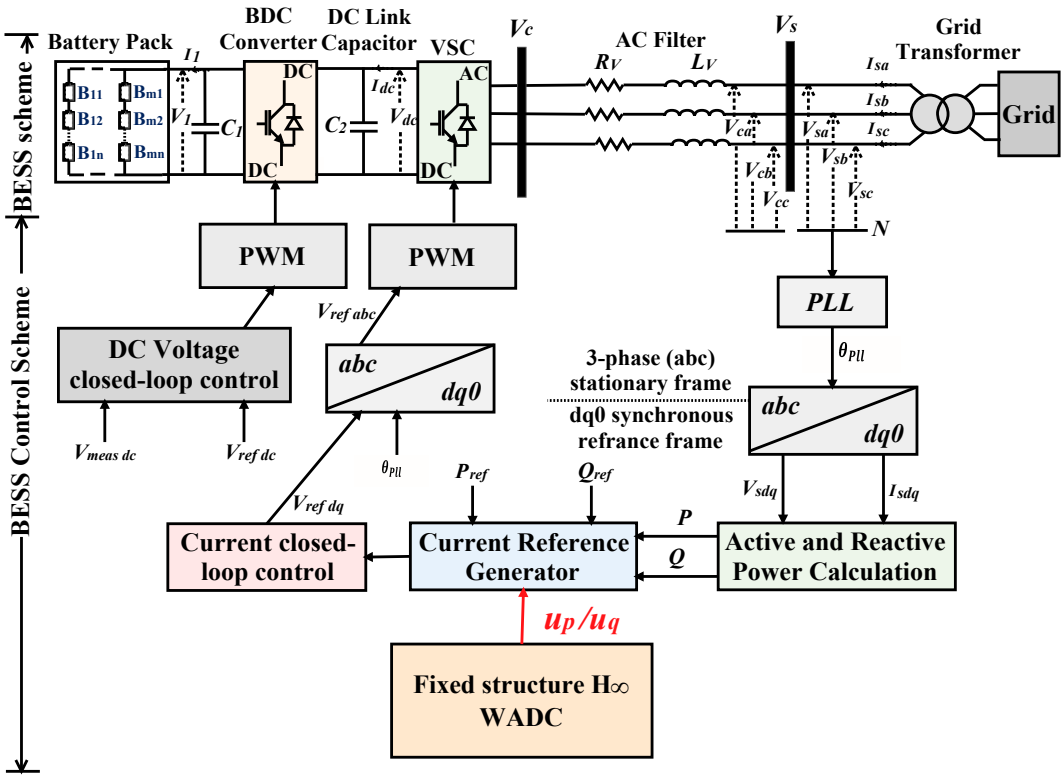

Figure 4.1: A Grid-Connected Battery Energy Storage System with Integrated Control.

4.2.1.2 DC-to-DC bidirectional converter model

In this study, the average model of a bidirectional converter in discharging and discontinuous conduction mode is used, and the DC-link current I_{dc} represents the VSC load. The weighted average dynamics model of the bidirectional converter in discharging mode for the switching period T_C is represented by [85].

$$\begin{cases} \dfrac{dI_L}{dt} = 0 - \dfrac{V_1}{L} - \dfrac{(1-\alpha_1)}{L} V_{dc} \\ \dfrac{dV_1}{dt} = -\dfrac{I_L}{C_1} - \dfrac{V_1}{C_1 R_b} + \dfrac{V_b}{C_1 R_b} \\ \dfrac{V_{dc}}{dt} = -\dfrac{(1-\alpha_1)}{C_2} I_L + \dfrac{I_{dc}}{C_2} \end{cases} \tag{4.1}$$

where V_1 is the battery pack terminal voltage, I_L is the inductor current, I_{dc} is the dc-link current, V_{dc} is the dc-link voltage, V_b is the battery cell voltage, R_b is the battery's internal resistance, bidirectional converter duty cycle is denoted by α_1 and its capacitance and inductance are designated by C_1,C_2, and L, respectively.

4.2.1.3 Voltage source converter model

The dynamics of the VSC, can be represented using the dq equations as follows [86] :

$$\begin{cases} L_V \dfrac{dI_{cd}}{dt} = (V_{cd} - V_{sd} - R_V I_{cd} + \omega_0 L_V I_{cq}) \\ L_V \dfrac{dI_{cq}}{dt} = (V_{cq} - V_{sq} - R_V I_{cq} - \omega_0 L_V I_{cd}) \end{cases} \tag{4.2}$$

where the VSC's dq reference frame voltages are $V_{cd} = 0.5 m_d V_{dc}$ and $V_{cq} = 0.5 m_q V_{dc}$. m_d and m_q are the modulation index of VSC in dq reference frame. V_s,V_c, and I_c represents the grid voltage, VSC voltage, and current, respectively. The aggregated inductance and resistance of the VSC, transformer, and filter are L_V, R_V.

4.2.1.4 Control approach for grid-integrated BESS

The commonly employed two-level control approach for grid-integrated BESS is depicted in Fig. 4.2. The primary level control is responsible for sustaining the constant DC-link voltage (V_{dc}) and the voltage level (V_{sd}) at the coupling point. The dq-axis reference current (I_{dqref}) generating for the primary-level control is given as

$$\begin{cases} I_{cdref} = (P_{sref} - P_s + u_p)\left(K_{pp} + \dfrac{K_{ip}}{s}\right) \\ I_{cqref} = (Q_{sref} - Q_s + u_q)\left(K_{pq} + \dfrac{K_{iq}}{s}\right) \end{cases} \tag{4.3}$$

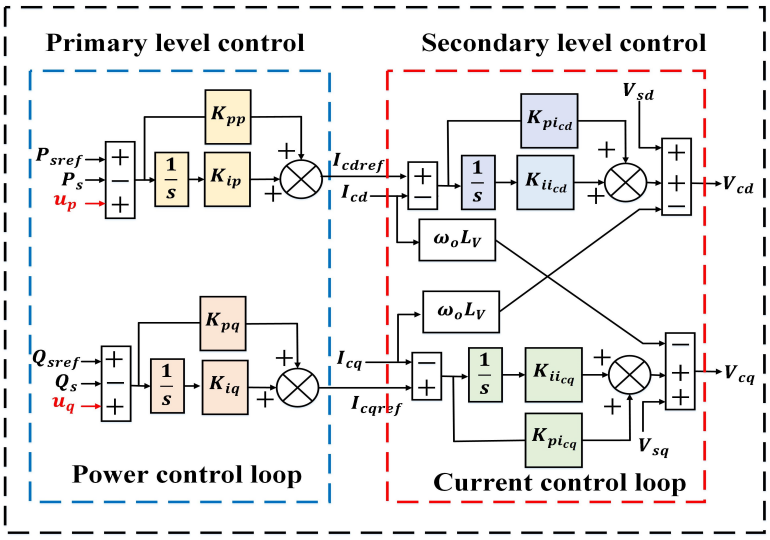

Figure 4.2: Control strategy for Battery Energy Storage System.

where u_p and u_q are the damping control signal of the WADC and K_{pp}, K_{pq}, K_{ip}, and K_{iq} are the PI controller gain coefficients of the primary level controller of the BESS.

The primary goal at the secondary level of the control strategy is to control power at the BESS integration point. This control is achieved by adjusting the VSC's modulation index (m_{dq}). Voltage-Oriented Control (VOC), which is one of the control methods, is demonstrated in[87]. VOC operates to convert the 3-phase (abc) signal stationary frame to the $dq0$-axis synchronous reference frame and vice versa. A Phase-Locked Loop (PLL) is used to measure angle $\theta_{pll} = \tan^{-1}\left(\frac{V_{sd}}{V_{sq}}\right)$, at the point of BESS integration. If $V_{sd} = V_s$ and $V_{sq} = 0$, direct axis voltage V_{sd} is then aligned with the grid voltage V_s to accomplish VOC. Now, the grid's active and reactive power that BESS delivers may be calculated as

$$\begin{cases} P_s = 1.5(V_{sd}I_{cd} + V_{sq}I_{cq}) = 1.5V_{sd}I_{cd} \\ \\ Q_s = 1.5(V_{sq}I_{cd} - V_{sd}I_{cq}) = -1.5V_{sd}I_{cq} \end{cases} \tag{4.4}$$

Under the lossless condition, active power received at the AC side of the VSC should be equivalent to active power delivered from the dc side of the VSC. $P_s = 1.5V_{sd}I_{cd} = V_{dc}I_{dc}$, thus current injected by DC-to DC bidirectional converter is $I_{dc} = 1.5\left(\frac{V_{sd}I_{cd}}{V_{dc}}\right)$. The currents along the q and d-axis are cross-coupled, which means that the I_{cq} depends on the I_{cd} and vice versa. Thus, as seen in Fig. 4.2, the decoupled controller came into the picture.

4.2.2 Small-signal analysis

This work aims to design a WADC for a BESS to improve the damping performance of LFO in the power system. Power flows in each transmission network are considered the system's outputs, while the BESS primary level controllers, P_{sref} and Q_{sref}, are chosen as inputs. The entire system, including the BESS, is linearized for these inputs and outputs at the stable equilibrium point, and the state-space model of the system is described using (3.8) of chapter-3.

4.2.2.1 Time delay in feedback signals

The 2nd-order Pad'e approximation is used in this study to describe time delays, and it is given as [88]:

$$G_{(T_d)}(s) = \frac{-2T_d s + 6}{s^2T_d^2 + 4T_d s + 6} = \frac{\frac{-2}{T_d s} + \frac{6}{T_d^2}}{s^2 + \frac{4}{T_d s} + \frac{6}{T_d^2}} \tag{4.5}$$

where time delay is represented by T_d, and the state-space model from the above transfer function can be obtained using (3.10) of chapter-3.

The delay-free system model determined by (3.8) is considered in cascade with (3.10) to make a system with a time delay model represented by (3.11).

The relevant system, input, and output matrices of the power system model with time delay are obtained using (3.12) of chapter-3.

4.3 Approach for Choosing the Location, Control Loop, and Feedback Signal for BESS

4.3.1 Residue index

It is worth mentioning that residue analysis is well established in the literature to address damping controller position and feedback signal selection in the context of power system low-frequency oscillation study. However, the residue index is not discussed for power system operating conditions variations. This chapter aims to determine the best position for BESS and its damping control loop. The residue index is exploited for subsequent analysis.

The plant model's residue matrix can be derived using (3.8) of chapter-3 the transfer-function representation [83], as per following

$$G(s) = C(sI - A)^{-1}B = \sum_{i=1}^{e} \frac{R_i}{s - \lambda_i} \tag{4.6}$$

where R_i is the residue index of $G(s)$ associated with LFO mode-i, at eigenvalue λ_i which may be further written as

$$R_i = CM_iN_i^TB \tag{4.7}$$

where N_i^T and M_i are the left and the right eigenvector matrices related to the eigenvalue λ_i , respectively. Both are the ith element of the modal matrix and are associated with the state matrix stated in (3.8) of chapter-3.

4.3.2 BESS selection approach

In a conventional approach, the location of the BESS installation, the feedback signal, and the control loop are selected [89] as follows:

$$M_p = Max[(R_i(\rho, \gamma_0)] \tag{4.8}$$

where ρ is the set of each candidate's installation positions, feedback signals, and control loops, M_p is the consequence of the choice, $M_p \in \rho$, and γ_0 is the steady-state operating condition.

The residue index will vary under various operating scenarios even though the installation position, feedback signal, and control loop are all the same. Therefore, (4.8) isn't always the perfect approach under a changing operating scenario.

To overcome the problem of the conventional approach described in (4.8), an alternative approach is proposed in this work for choosing the BESS installation position, feedback signal, and control loop under the variation of system operating conditions as follows:

$$M_p = Max[min(R_i(\rho, \Phi(\gamma)))] \tag{4.9}$$

where $\Phi(\gamma)$ is a collection of various operating conditions, such as an increase or decrease in load and a change in network configuration. Depending on the inter-area oscillation mode of interest, there is a minimal magnitude of residue index under various operating conditions for each element of ρ. The operating condition γ_p that results in minimum residue magnitude is considered optimal operating condition. M_p (i.e., optimal BESS location, feedback signal and control loop) is decided based on maximal of minimum residues under different values of ρ for the optimal operating condition γ_p. The selection results from M_p corresponds to least efficient damping in the i^{th} inter-area mode at the operating condition $\gamma_p \in \Phi(\gamma)$, according to (4.9). As a result, if we select γ_p as the operating condition in the system to design the BESS-based damping controller, an efficient design at M_p can confirm its efficacy for all other operating conditions in $\Phi(\gamma)$. Therefore, (4.9) is a robust approach for choosing the BESS installation position, the feedback signals, and the control loop.

4.4 Design of WADC Using Fixed Structure Control Scheme

4.4.1 Framework of fixed structure control scheme

The fixed-structure controller, the standard form model, is shown in Fig. 4.3 and consists of two primary components:

1. All non-tunable (fixed) blocks in the control system are combined in the linear time-invariant plant model $P(s)$.

2. A structured controller that combines all tunable elements of the controller is $K(s)$ = Diag$(K_1(s), ..., K_N(s))$. It is assumed that each control element $K_j(s)$ is linearly time-invariant and has a predetermined structure.

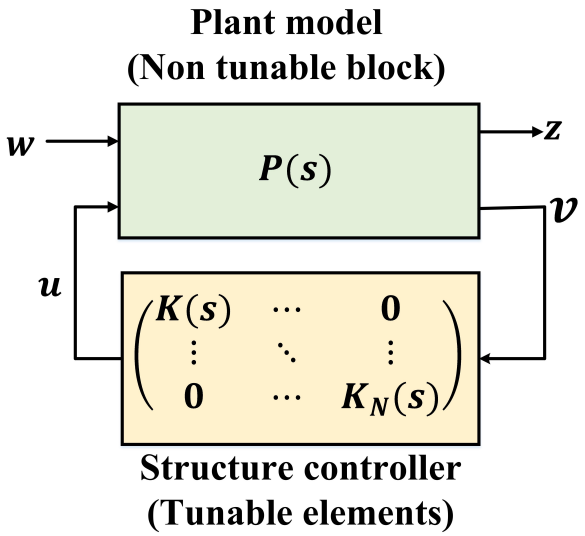

Figure 4.3: Fixed-structure controller standard form model.

The system's external inputs, such as disturbances and reference signals, are collected in w, while its performance-related outputs, such as error signals, are collected in z. The linear fractional transformation yields the closed-loop transfer function from w to z, denoted $Fl(P(s), K(s))$, as follows [90]:

$$T_{zw} = Fl(P, K) = P_{zw} + P_{zu}K(I - P_{vu}K)^{-1}P_{vw} \tag{4.10}$$

4.4.2 Fixed-structure H_∞ controller synthesis

The fixed-structure H_∞ control scheme for the BESS is shown in Fig. 4.4. In this study, the design of the damping controller for the BESS considers P_{sref} and Q_{sref} as external or disturbance inputs (w), while $P_{sref} - P_s$ and $Q_{sref} - Q_s$ are taken as regulated outputs (z). The power flow through the transmission network (P_{Line}) is used as the measured output (v), which is obtained using a PMU. A communication time delay is modeled using a 2nd-order Padé approximation, linked with the feedback signal of the damping controller. The control signals u_p and u_q are generated by the damping controller and connected to the active and reactive power outer control loops of the BESS, as shown in Fig. 4.2. The outer control loop of the BESS (i.e., the active and reactive power control loops) consists of a PI controller, as discussed in Section 4.2.1.4. The reference current signals I_{cdref} and I_{cqref} are generated by the outer control loop to regulate the output voltage of the VSC (V_{cd} and V_{cq}) to control the voltage at the point where the BESS is connected to the power system.

The design objective is to minimize the H_∞ norm of $Fl(P(s), K(s))$. The solution objective for optimal H_∞ problem is to identify an internally stabilizing controller $K(s)$ where $\|Fl(P(s), K(s))\|_\infty$ is reduced [90].

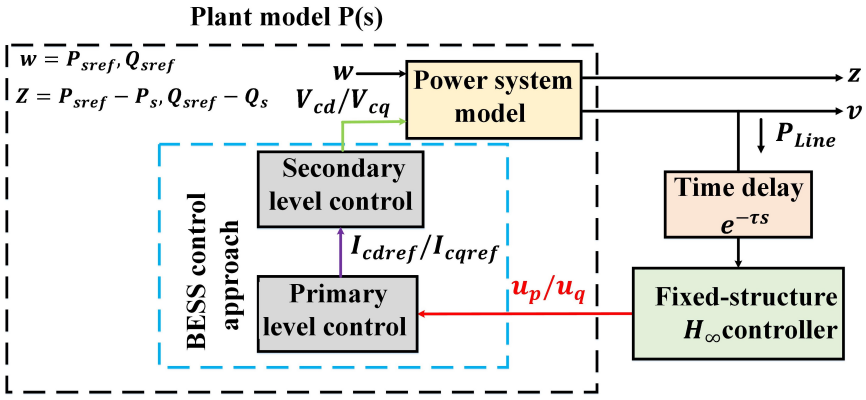

Figure 4.4: Fixed-structure H_∞ control scheme for BESS.

PSS is considered a fixed-structure damping controller, including a controller gain, a washout filter, and a phase compensation filter. Using parametric models for such components is only reasonable, given that our strategy is optimization-based. For instance, six scalars $K_c, T_{wc}, T_{1c}, T_{2c}, T_{3c}$, and T_{4c} can be used to parameterize a PSS as:

$$K(s) = K_c \left(\frac{sT_{wc}}{sT_{wc}+1}\right)\left(\frac{sT_{1c}+1}{sT_{2c}+1}\right)\left(\frac{sT_{3c}+1}{sT_{4c}+1}\right) \tag{4.11}$$

The optimization problem of fixed-structure H_∞ controller is solved using nonsmooth optimization. The objective is to identify optimal fixed-structure controller $K(s)$ design parameters that minimize the H_∞ norm considering all internal stability constraints [91].

$$\begin{aligned} &\underset{K(s)}{\text{minimize}} \|Fl(P(s), K(s))\|_\infty \iff \\ &\underset{x \in \Re^k}{\text{minimize}} \max_{\omega[0,\infty]} \bar{\sigma}(Fl(P(j\omega), x)) \end{aligned} \tag{4.12}$$

where the vector x collects all the tunable parameters in fixed-structure controller $K(s)$. The nonsmooth optimization-based control problem is solved using MATLAB-based *hinfstruct* function.

4.4.3 Procedure to design fixed-structure WADC

1. Linearize the entire power system at robust operating condition γ_p.

2. Small-signal analysis is used to identify the system's inter-area oscillation modes and the dominant inter-area oscillation modes are then determined based on frequency and damping ratio.

3. Use residue analysis to identify the appropriate feedback signal with a time delay for the dominant inter-area oscillation mode.

4. The full-order power system is converted to a reduced-order system model using the Schur model reduction method [44] to design WADC for BESS.

5. The reduced-order system is converted into the standard model form, which has a non-tunable block (plant model), and tunable sections (structured controller), in the fixed-structure control design problem.

6. In this study, PSS is regarded as a fixed-structure and parametric models are used to characterize the structure of each tunable element of fixed-structure controller $K(s)$.

7. The fixed-structure controller $K(s)$ design parameters minimize the H_∞ norm $\|Fl(P(s), K(s))\|_\infty < 1$ while adhering to internal stability constraints.

8. The fixed-structure controller $K(s)$ parameters are tuned using the *hinfstruct* function in MATLAB.

9. Validate the proposed WADC system's performance in various operating scenarios.

4.4.4 Flowchart of the proposed scheme

The flowchart in Fig. 4.5 shows the proposed scheme.

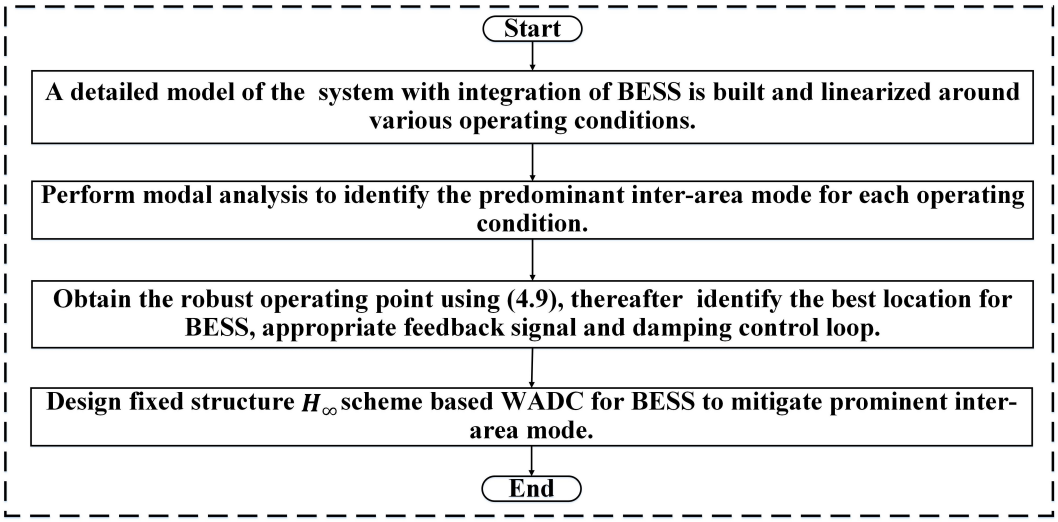

Figure 4.5: Flowchart of the proposed scheme.

4.5 Validation on Modified New England Ten-Machine Benchmark System

4.5.1 Study system description and small signal analysis

The modified New England 39-bus benchmark power system is depicted in Fig. 4.6. This test system consists of 10 synchronous generators, 39 buses, 46 transmission lines, 21 loads, 12 transformers, and six inter-area tie lines, with a total generation capacity of 6248.9 MW. The system base is set at 100 MVA and 60 Hz, with the power ratings of each generator being different, as discussed in [92]. The primary and secondary voltage ratings of each transformer connecting the generator buses in the IEEE 39-bus system are 11.3 kV and 345 kV, respectively. Additionally, each bus connected to the transmission lines operates at a voltage rating of 345 kV. The details of the study system are given in Appendix-C. This test system is divided into three areas: SG1-SG3 are in Area-1, SG4-SG7 are in Area-2, and SG8-SG10 are in Area-3. Moreover, every excitation system

of SGs equipped with local PSS, excluding SGs G1, G5, G7, and G8, has a gain that is 25 times greater than the PSS data obtained from [92].

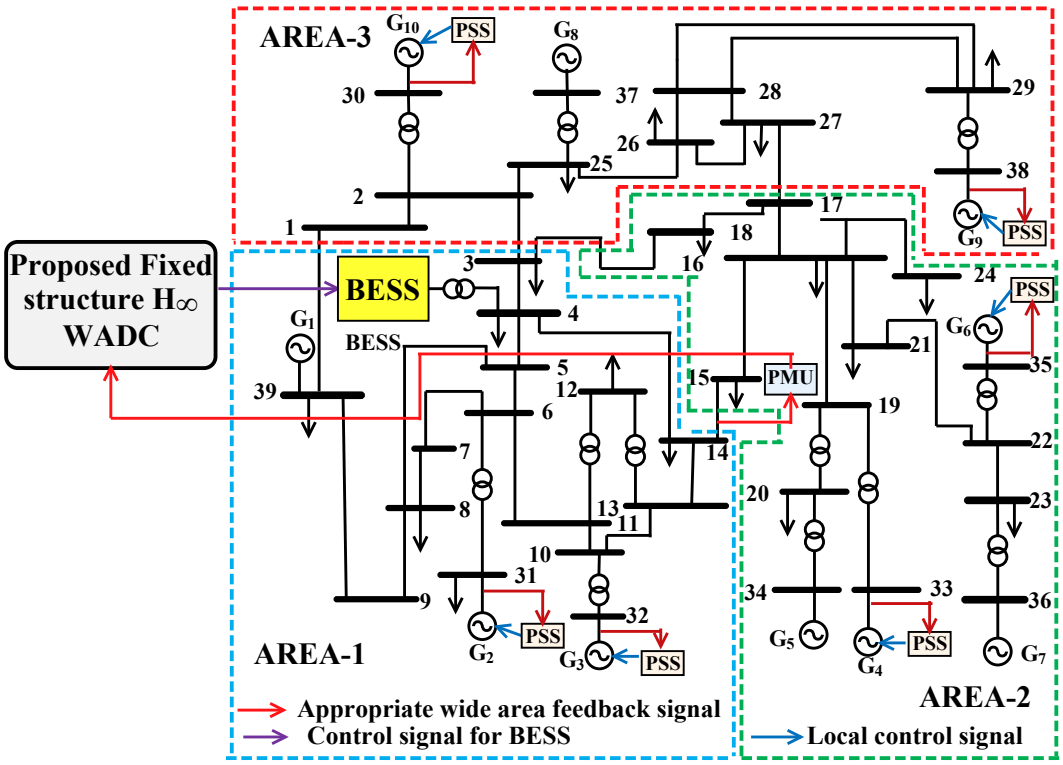

Figure 4.6: Single-line diagram of the New England 39-bus system integrated with BESS.

In this work, we differentiate between two configurations in a multi-machine power system: one without BESS, termed the base case (BC), and the other incorporating BESS, known as case 1 (CS1). The main objective is to assess the system's damping ability to mitigate inter-area oscillations across various operating conditions. Table 4.1 provides a comprehensive overview of the various operational conditions explored in this study, identified as γ_{p1}, γ_{p2}, γ_{p3}, and γ_{p4}, respectively. The small-signal analysis is conducted for the base case configuration of the study test system to examine the prominent inter-area oscillation mode under different operational scenarios. The results are summarized in Table 4.1, focusing primarily on the dominant inter-area oscillation mode while other low-frequency oscillation modes are not listed.

Furthermore, the SGs in Area-3 actively participate in the dominant inter-area oscillation mode in the base case under different operating conditions, as shown in Fig. 4.7. So, at bus-27 (Area-3), a 50 MW BESS is incorporated with the study test system to provide power requirements under any additional loading scenario. The parameters of BESS are taken from [17]. In this simulation analysis, BESS operates in discharging

Table 4.1: Power system operating conditions

$\Phi(\gamma_p)$	**System operating conditions description**
γ_{p1}	Active and reactive power of loads at the Area-1 (Bus-31 & Bus-39) increase by 10%
γ_{p2}	Active and reactive power of loads at the Area-2 (Bus-20 & Bus-23) increase by 10%
γ_{p3}	Active and reactive power of loads at the Area-3 (Bus-25 & Bus-29) decrease by 10%
γ_{p4}	The permanent outage of the inter-area line between Bus-2 & Bus-3

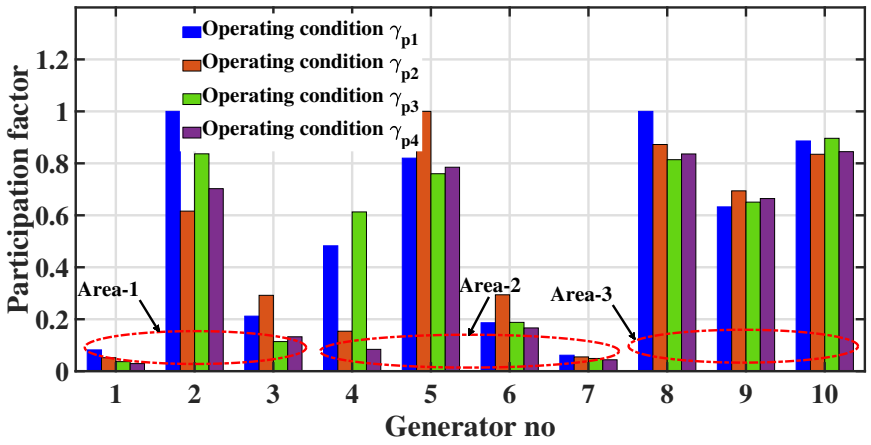

Figure 4.7: Participation factor of synchronous generators in the dominant oscillation mode in the base case under various operating conditions.

mode, with the initial State of Charge (SOC) of BESS being taken as 80%. Under normal operating conditions, a BESS is integrated on Bus-27, and this system has an inter-area mode present as ($\lambda_i = -0.2696 \pm j3.9107$). Furthermore, for case 1, Table 4.1 comprehensively presents the dominant inter-area oscillation mode and the residue index of the system across various operating conditions, providing valuable insights into the system's dynamic behaviour.

In Table 4.2, in the base case, we observe that the damping ratio of mode M1 is obtained as 4.70%, which is increased to 5.61% in case1 under γ_{p1} operating condition. However, in operating condition γ_{p2}, the damping ratio of mode M2 is obtained as 6.26%, which is reduced to 5.96% in case 1. The damping ratios of modes M3 and M4 are obtained as 6.54% and 6.46% in base case under operating conditions γ_{p3}, and γ_{p4}, these

ratios again increased to 6.87% and 6.45% in case 1. So, it can be observed that the damping performance in case 1 exhibits a marginal improvement when compared to the base case for the dominant inter-area mode across different operating conditions.

Table 4.2: Damping ratio of the study system in the base case and case1 for different operating conditions

$\boldsymbol{\Phi(\gamma_p)}$	**Mode**	**Damping ratio in base case**	**Damping ratio in case 1**	**Residue Index of case 1**
γ_{p1}	M1	$-0.252 \pm i5.366$ ($\xi = 4.70\%$, $f = 0.85$ Hz)	$-0.230 \pm i4.095$ ($\xi = 5.61\%$, $f = 0.65$ Hz)	$0.0189\angle \mp 13.34^\circ$
γ_{p2}	M2	$-0.339 \pm i5.408$ ($\xi = 6.26\%$, $f = 0.86$ Hz)	$-0.305 \pm i5.116$ ($\xi = 5.96\%$, $f = 0.81$ Hz)	$0.0042\angle \pm 103.72^\circ$
γ_{p3}	M3	$-0.352 \pm i5.376$ ($\xi = 6.54\%$, $f = 0.85$ Hz)	$-0.269 \pm i3.910$ ($\xi = 6.87\%$, $f = 0.62$ Hz)	$0.0210\angle \pm 146.35^\circ$
$\boldsymbol{\gamma_{p4}}$	**M4**	$\boldsymbol{-0.353 \pm i5.452}$ ($\boldsymbol{\xi = 6.46\%}$, $\boldsymbol{f = 0.86}$**Hz**)	$\boldsymbol{-0.33 \pm i5.154}$ ($\boldsymbol{\xi = 6.45\%}$, $\boldsymbol{f = 0.82}$**Hz**)	$\boldsymbol{0.0018\angle \mp 48.16^\circ}$

As shown in Table 4.2, the minimal magnitude of the residue index (0.0018) is obtained under the operating condition γ_{p4}. Therefore, in this research, operating condition γ_{p4} is chosen for designing the WADC for the BESS.

4.5.2 Frequency response of study system

The frequency response (Bode plot) of the study system under steady-state conditions, both without and with BESS, are shown in Fig. 4.8(a) and (b), respectively. In the system without BESS, a gain margin of 32.4 dB is observed at a phase crossover frequency of 16.1 rad/sec, along with a phase margin of 49 deg at a gain crossover frequency of 0.892 rad/sec. Conversely, the system with BESS exhibits a gain margin of 45.6 dB at a phase crossover frequency of 20.4 rad/sec and a phase margin of 107.5 deg at a gain crossover frequency of 0.796 rad/sec. These results indicate that incorporating BESS increases both

the gain and phase margins of the system. Consequently, the damping performance and overall stability of the system are enhanced compared to the system without BESS.

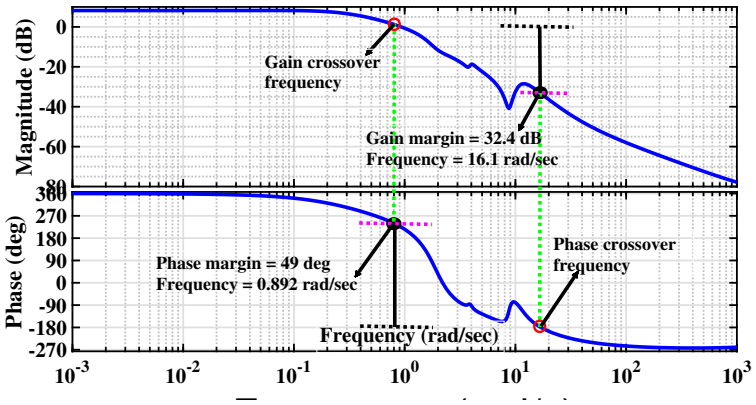

(a)

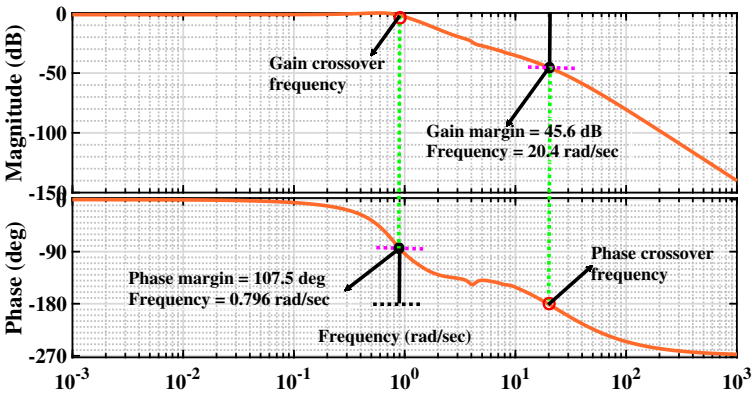

(b)

Figure 4.8: Bode plot of the study system: (a) Without BESS, (b) With BESS.

4.5.3 Choice of BESS installation position, feedback signal, and damping control loop

The candidate group $\Omega(\rho)$ is chosen in this work, as shown in Table 4.3, for analyzing the impact of grid-connected BESS in system inter-area oscillation mode under the variation of power system operating conditions.

Under the operating condition γ_{p4}, the residue index magnitude of the system is depicted in Fig. 4.9. From Fig. 4.9, the maximal magnitude of the residue index is 0.0795 at candidate group ρ_9 (i.e., reactive power control loop). The candidate group ρ_9 is

the best choice by the conventional approach according to (4.8); in this case, the BESS installation position at Bus-4 (Area-1), the feedback signal is the power flow over an inter-area tie line P_{15-14} (between Areas 2 to 3), and the damping control loop is the reactive loop of BESS.

Table 4.3: Candidate group of study system

Candidate group $\Omega(\rho)$	**Collection of candidate groups**
Candidate BESS location	Bus-4 (Area-1), Bus-22 (Area-2), & Bus-27 (Area-3)
Candidate damping control loops	Active & reactive power control loops
Candidate feedback signals of the damping controller	Power flow through lines P_{26-27}, P_{27-17} (between Area-3 to Area-2), P_{1-39} (between Area-3 to Area-1), P_{15-14} (between Area-2 to Area-1), & rotor speed deviation $\Delta\omega_{4-8}$ (Area-2 to Area-3)

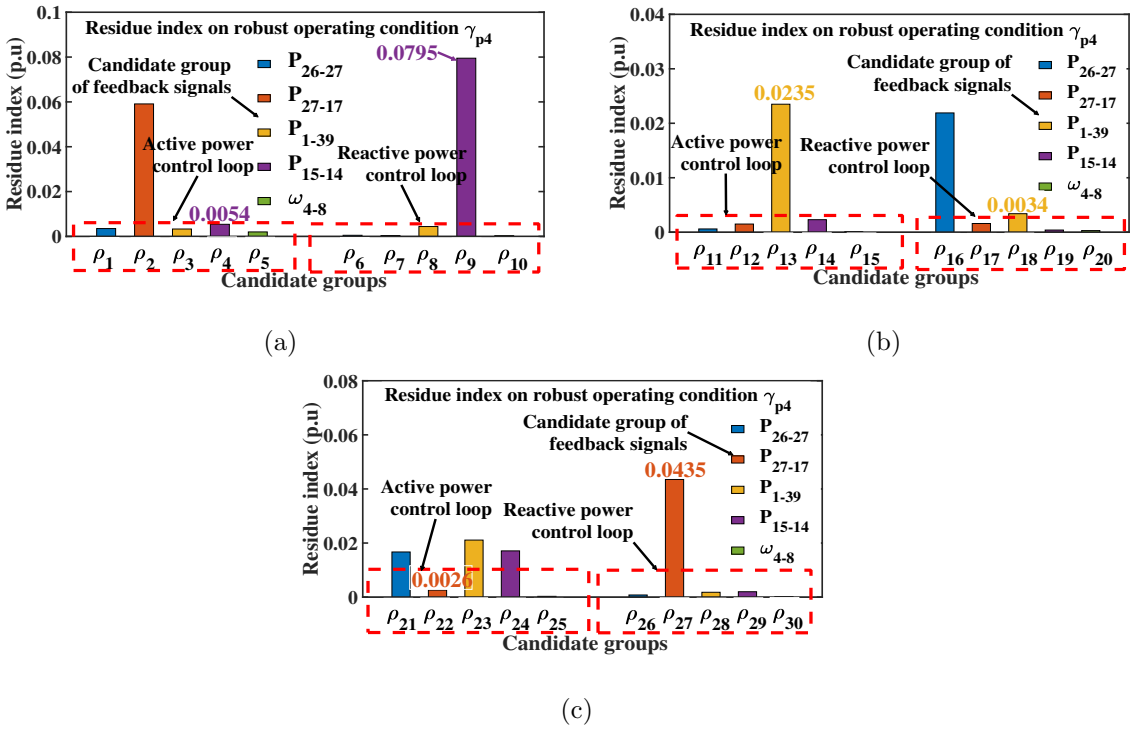

Figure 4.9: Residue index of study system under operating condition γ_{p4}.(a) BESS installed on Bus-4, (b) BESS installed on Bus-22, and (c) BESS installed on Bus-27.

From Fig. 4.9, the maximal of all the minimal magnitude of residue index is 0.0054 at candidate group ρ_4 (i.e., active power control loop). The candidate group ρ_4 is the

best choice by the robust approach according to (4.9); in this case, the BESS installation position is at Bus-4, the feedback signal is the power flow over an inter-area tie line P_{15-14}, and the active power loop of BESS is the damping control loop.

According to Fig. 4.9 (a, b, and c), we draw conclusions about this analysis.

1. The robust choice between each candidate in $\Omega(\rho)$ is the candidate group ρ_4. The minimal magnitude of the residue index of the candidate group ρ_4 is the maximal in each lower residue index magnitude of candidates in $\Omega(\rho)$. Thus, candidate group ρ_4 is the best choice found based on (4.9), which states that the BESS should be placed at Bus-4, the feedback signal is the power flow over an inter-area tie line P_{15-14}, and the active power loop of BESS is the damping control loop.

2. BESS installation on Bus-4 is superior to Bus-22 and Bus-27 .

3. The feedback signal P_{15-14} is superior compared to the feedback signals P_{26-27}, P_{27-17}, P_{1-39} and ω_{4-8}.

4.5.4 Design of BESS-based WADC

The first stage in designing the proposed WADC for BESS is selecting the damping controller location and the appropriate feedback signal to improve the system's damping performance under various operating conditions. The damping control loop and feedback signal are selected using the robust selection approach outlined in Section 4.3.2. From Fig. 4.9, it is determined that the active power control loop of the BESS is the optimal location to position the WADC. Furthermore, the power flow through the inter-area line P_{15-14} is the appropriate feedback signal for designing the WADC for the BESS. It is considered that the PMU is deployed on bus 15 of the test system to get the WADC feedback signal, and the PMU utilize IEEE C37.118.2 protocol for real-time data streaming. PMUs capture voltage, current, and frequency at high sampling rates (240 samples per second) to monitor the dynamic behaviour of the New England 39-bus practical system.

In this research, we have also accounted for the communication delays in the feedback signal, i.e., minimum and maximum time delays of 100 ms and 150 ms, respectively. With P_{15-14} as the output of the plant model and P_{sref} as the input for the operating condition γ_{p4} with a 100 ms time delay in feedback signals, the order of the system is found to be

139. This higher-order system is further reduced to a 12^{th}-order system using the Schur model reduction approach [44] for case CS1 to reduce the WADC design's complexity. The frequency response of the 12^{th}-order reduced system is approximately the same as the full-order system in the frequency range of (0.1-2) Hz, as shown in Fig. 4.10. The reduced order system contains the significant inter-area oscillation mode M4 under the operating condition γ_{p4}.

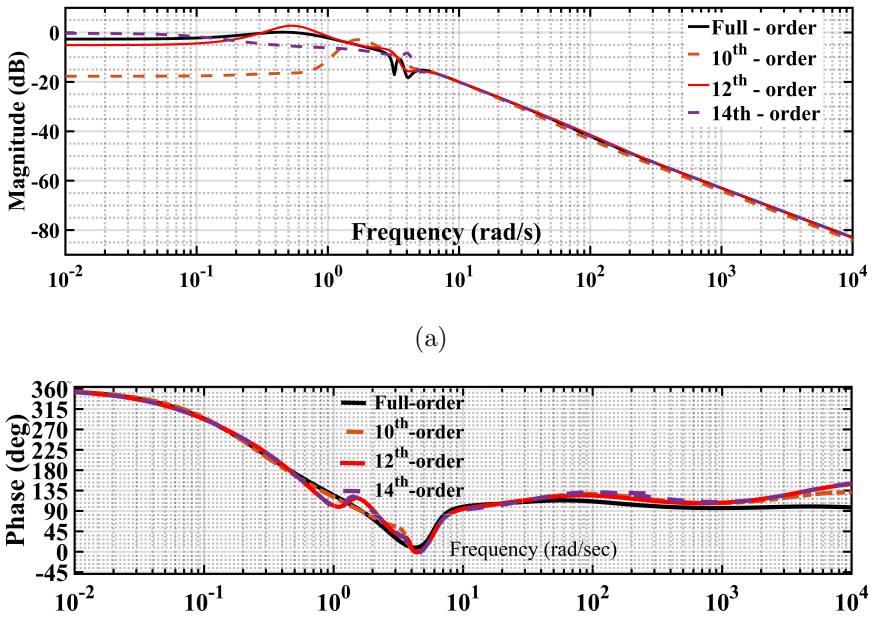

(a)

(b)

Figure 4.10: Frequency responses of the modified New England 39-bus system of full-order and reduced-order system under operating condition γ_{p4}.

4.5.4.1 Design of fixed-structure H_∞ scheme based WADC for BESS

The design procedure for the fixed-structure H_∞ scheme-based WADC is provided in Section 4.4. This study designs the proposed WADC for the BESS under the operating condition γ_{p4} in the candidate group ρ_4, where the WADC is linked to the active power control loop of the BESS. The objective is to increase the damping ratio of the relevant inter-area oscillation modes, M1 to M4, of the study system in case CS1. The *hinfstruct* function in MATLAB is used to tune the parameter of the fixed-structure damping controller (i.e., PSS). After almost 31 iterations, the H_∞ program based on nonsmooth structure optimization converges to its optimum closed-loop gain value of 1.31, which means that the H_∞ norm is almost satisfied. The damping controller's tuned parame-

ters are $K_c = 0.851, T_{wc} = 10, T_{1c} = 0.654, T_{2c} = 0.0134, T_{3c} = 0.567$, and $T_{4c} = 0.0135$, respectively.

Moreover, in this study, the fixed-structure H_∞ WADC designed for the BESS under the operating condition γ_{p4} in the candidate group ρ_9 (i.e., WADC is linked to the reactive power control loop of BESS), is compared with the proposed WADC in the candidate group ρ_4. The H_∞ norm is not satisfied since the nonsmooth structural optimization-based H_∞ program does not converge to a solution. The best closed-loop gain value of 2.31 after around 47 iterations with parameters of the damping controller are obtained to be $K_c = 1.738, T_{wc} = 10, T_{1c} = 0.451, T_{2c} = 0.0252, T_{3c} = 0.456$, and $T_{4c} = 0.0247$, respectively.

4.5.4.2 Performance evaluation of WADC

The proposed fixed-structure H_∞ scheme-based WADC's damping performance for the BESS is evaluated through modal analysis on the modified New England 39-bus system. The main objective is to evaluate the damping performance of the system in inter-area modes under various operating conditions. The damping performance of the dominant inter-area oscillation modes of the system wherein the WADC is associated with the candidate groups ρ_4 and ρ_9 of BESS are respectively shown in Tables 4.4 and 4.5. The damping performance of the dominant inter-area oscillation modes were also studied for the system integrated with an existing BESS-based Wide-Area Power System Stabilizer(WAPSS)[83]. The WAPSS is a single-input, single-output (SISO) structure that utilizes P_{15-14} as a feedback signal. This stabilizer is connected to the secondary control loop of the BESS. This WAPSS scheme is implemented on the candidate groups ρ_4 and ρ_9 of BESS to evaluate the damping performance in the practical study system inter-area oscillation modes under the operating condition γ_{p4}.

The 10% damping ratio is the threshold value to assess the proposed controller's effectiveness in the study system inter-area modes under different operating conditions. The damping ratio in the inter-area mode M4 with the 100 ms time delay in the feedback signal in BESS-based WAPSS [83] in candidate group ρ_4 is less than 10%, as depicted in Table 4.4. The damping of the concerned inter-area oscillation modes M1 to M4 is improved beyond 10% by the proposed fixed-structure H_∞ WADC. When the proposed WADC is installed on the candidate group ρ_9, the damping ratio of concerned inter-area

oscillation modes M1 to M3 is higher than 10%, except the single case of the inter-area oscillation Mode M4 with 150 ms time delay in feedback signal, where the damping ratio is slightly lower than 10%. The BESS-based WAPSS [83] is installed on the candidate group ρ_9; the damping ratio of concerned inter-area oscillation modes M1 to M4 is lower than 10% (see Table 4.5).

Table 4.4: Eigenvalue of system inter-area oscillation modes with WADCs in the candidate group ρ_4 of BESS

$\boldsymbol{\Phi(\gamma_p)}$	**Mode**	$\boldsymbol{T_d(ms)}$	**BESS-based WAPSS [83]**	**Proposed fixed structure WADC**
γ_{p1}	M1	100	$-0.441 \pm i3.677$ ($\xi = 11.93\%$)	$-0.553 \pm i3.654$ ($\xi = 14.98\%$)
		150	$-0.415 \pm i4.069$ ($\xi = 10.16\%$)	$-0.527 \pm i3.749$ ($\xi = 13.92\%$)
γ_{p2}	M2	100	$-0.443 \pm i3.993$ ($\xi = 11.03\%$)	$-0.560 \pm i3.739$ ($\xi = 14.81\%$)
		150	$-0.455 \pm i4.063$ ($\xi = 11.14\%$)	$-0.538 \pm i3.707$ ($\xi = 14.38\%$)
γ_{p3}	M3	100	$-0.465 \pm i3.667$ ($\xi = 12.59\%$)	$-0.537 \pm i3.789$ ($\xi = 14.05\%$)
		150	$-0.448 \pm i3.978$ ($\xi = 11.19\%$)	$-0.556 \pm i3.715$ ($\xi = 14.80\%$)
$\boldsymbol{\gamma_{p4}}$	**M4**	**100**	$\boldsymbol{-0.371 \pm i3.751}$ ($\boldsymbol{\xi = 9.85\%}$)	$\boldsymbol{-0.511 \pm i3.617}$ ($\boldsymbol{\xi = 14.01\%}$)
		150	$\boldsymbol{-0.530 \pm i5.081}$ ($\boldsymbol{\xi = 10.37\%}$)	$\boldsymbol{-0.527 \pm i3.749}$ ($\boldsymbol{\xi = 13.92\%}$)

In the presence of contingencies and uncertainty associated with communication time delays in the feedback signal, the proposed fixed-structure H_∞ scheme-based WADC functions robustly for the designed parameters. When time delay constraints are taken into consideration, the proposed WADC for BESS is capable of maintaining at least a 10% damping ratio in prominent inter-area oscillation modes. In contrast, the BESS-based WAPSS [83] is incapable of providing enough damping for critical inter-area oscillation modes.

Table 4.5: Eigenvalue of system inter-area oscillation modes with WADCs in the candidate group ρ_9 of BESS

$\Phi(\gamma_p)$	Mode	$T_d(ms)$	BESS-based WAPSS [83]	Proposed fixed structure WADC
γ_{p1}	M1	100	$-0.476 \pm i4.936$ ($\xi = 9.61\%$)	$-0.420 \pm i4.039$ ($\xi = 10.36\%$)
		150	$-0.469 \pm i4.956$ ($\xi = 9.425\%$)	$-0.371 \pm i3.528$ ($\xi = 10.46\%$)
γ_{p2}	M2	100	$-0.346 \pm i4.147$ ($\xi = 8.33\%$)	$-0.450 \pm i3.854$ ($\xi = 11.6\%$)
		150	$-0.443 \pm i4.960$ ($\xi = 8.71\%$)	$-0.439 \pm i3.685$ ($\xi = 11.84\%$)
γ_{p3}	M3	100	$-0.368 \pm i4.027$ ($\xi = 9.10\%$)	$-0.384 \pm i3.619$ ($\xi = 10.55\%$)
		150	$-0.359 \pm i3.838$ ($\xi = 9.32\%$)	$-0.373 \pm i3.469$ ($\xi = 10.71\%$)
$\boldsymbol{\gamma_{p4}}$	M4	**100**	$\mathbf{-0.406 \pm i4.939}$ ($\boldsymbol{\xi = 8.19\%}$)	$\mathbf{-0.400 \pm i3.942}$ ($\boldsymbol{\xi = 10.19\%}$)
		150	$\mathbf{-0.420 \pm i4.946}$ ($\boldsymbol{\xi = 8.47\%}$)	$\mathbf{-0.359 \pm i3.838}$ ($\boldsymbol{\xi = 9.32\%}$)

4.6 Validation of Dynamic Simulation on the Real-Time Digital Simulator

The dynamic simulation of the modified New England 39-bus system with proposed fixed-structure H_∞ WADC for BESS is carried out on RTDS using the graphical user interface of RSCAD FX 1.3. The Real-Time Digital Simulation framework is depicted in Fig. 2.14 of chapter-2.

The dynamic simulation of the studied test system is carried out to verify the efficacy of the proposed WADC for BESS and evaluate its performance under different operating scenarios. The different scenarios are simulated under following contingency cases:

- Scenario 1 (S1): A three-phase fault is applied at bus-20 in Area-2 at t = 3 sec for 100 ms.
- Scenario 2 (S2): A double line to fault is applied at t = 3 sec for 100 ms on the transmission line between buses 29 and 37 and considering the permanent outage

on the transmission line between buses 27 and 17 as well as buses 3 and 4.

- Scenario 3 (S3): Considering the variable communication time delay in the WADC feedback signal P_{15-14}, a line-to-ground fault is applied to the transmission line between buses 16 and 19 at t = 3 sec for 100 ms.

- Scenario 4 (S4): The integration of the solar photovoltaic system on bus-20 and the three-phase fault is applied at bus 38 at t = 3 sec for 100 ms.

Except for scenario S3, the simulation case for each scenario considers 100ms communication time delay in the proposed WADC's feedback signal P_{15-14} into account.

4.6.1 Scenario 1 (S1)

In this scenario, we evaluated the damping performance of proposed WADC for BESS in candidate groups ρ_4 (i.e., active control loop) and ρ_9 (i.e., reactive control loop) by conducting simulations under various operating conditions (see Table 4.1, γ_{p1} to γ_{p4}) of the practical study system. In this simulation scenario, the three-phase fault is applied at bus-20 in Area-2 at 3s with a fault duration of 100 ms to generate dynamic oscillations in the system.

The dynamic simulation response of the rotor speed deviation between SGs 4 and 2, and the DC link voltage (V_{dc}) of the BESS with the proposed WADC for BESS as well as for the WAPSS [83] in candidate group ρ_4 under different operating conditions are depicted in Fig. 4.11. This simulation response reveals that the SG rotor oscillation and BESS DC link voltage oscillation are better damped after the occurrence of a fault, reducing peak overshoot and settling time of the rotor oscillation and DC link voltage oscillation, compared to the BESS-based WAPSS [83]. In each operating condition (γ_{p1} to γ_{p4}), the settling time of the SG rotor oscillation and DC link voltage oscillation of BESS is less than 8 sec by the proposed WADC. Further, the peak overshoot of both the SG rotor oscillation and the DC link voltage of the BESS effectively reduced, as shown in Fig. 4.11.

Additionally, Fig. 4.12 illustrates the dynamic response of the proposed WADC as well as of WAPSS [83] for BESS in candidate group ρ_9. This simulation response includes the rotor speed deviation between SGs 4 and 2, and the DC link voltage of the

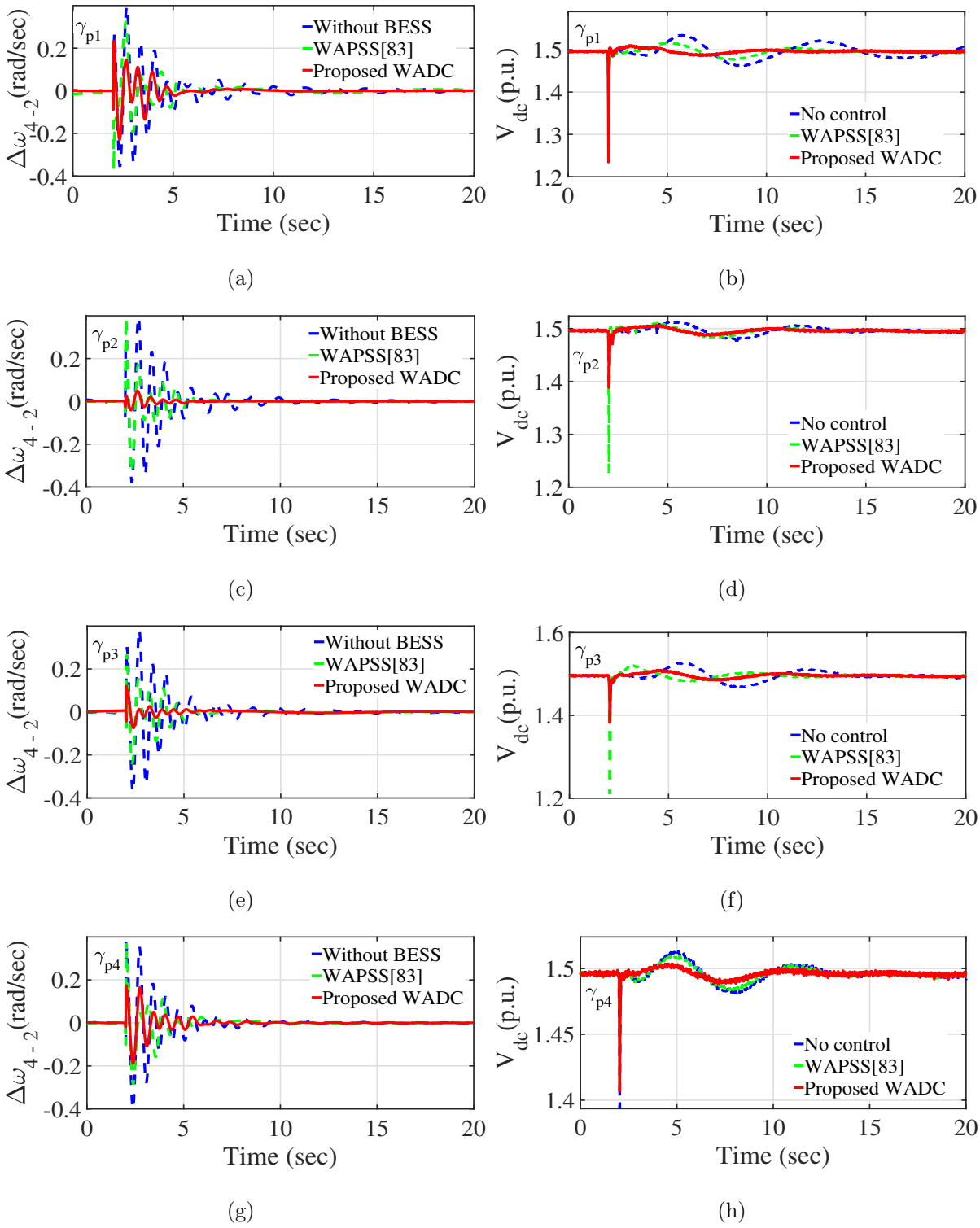

Figure 4.11: Dynamic response of the study system with a WADC for BESS in candidate group ρ_4 under various operating conditions: (a) $\Delta\omega_{4-2}$ under γ_{p1}, (b) V_{dc} under γ_{p1}, (c) $\Delta\omega_{4-2}$ under γ_{p2}, (d) V_{dc} under γ_{p2},(e) $\Delta\omega_{4-2}$ under γ_{p3},(f) V_{dc} under γ_{p3}, (g) $\Delta\omega_{4-2}$ under γ_{p4}, and (h) V_{dc} under γ_{p4}.

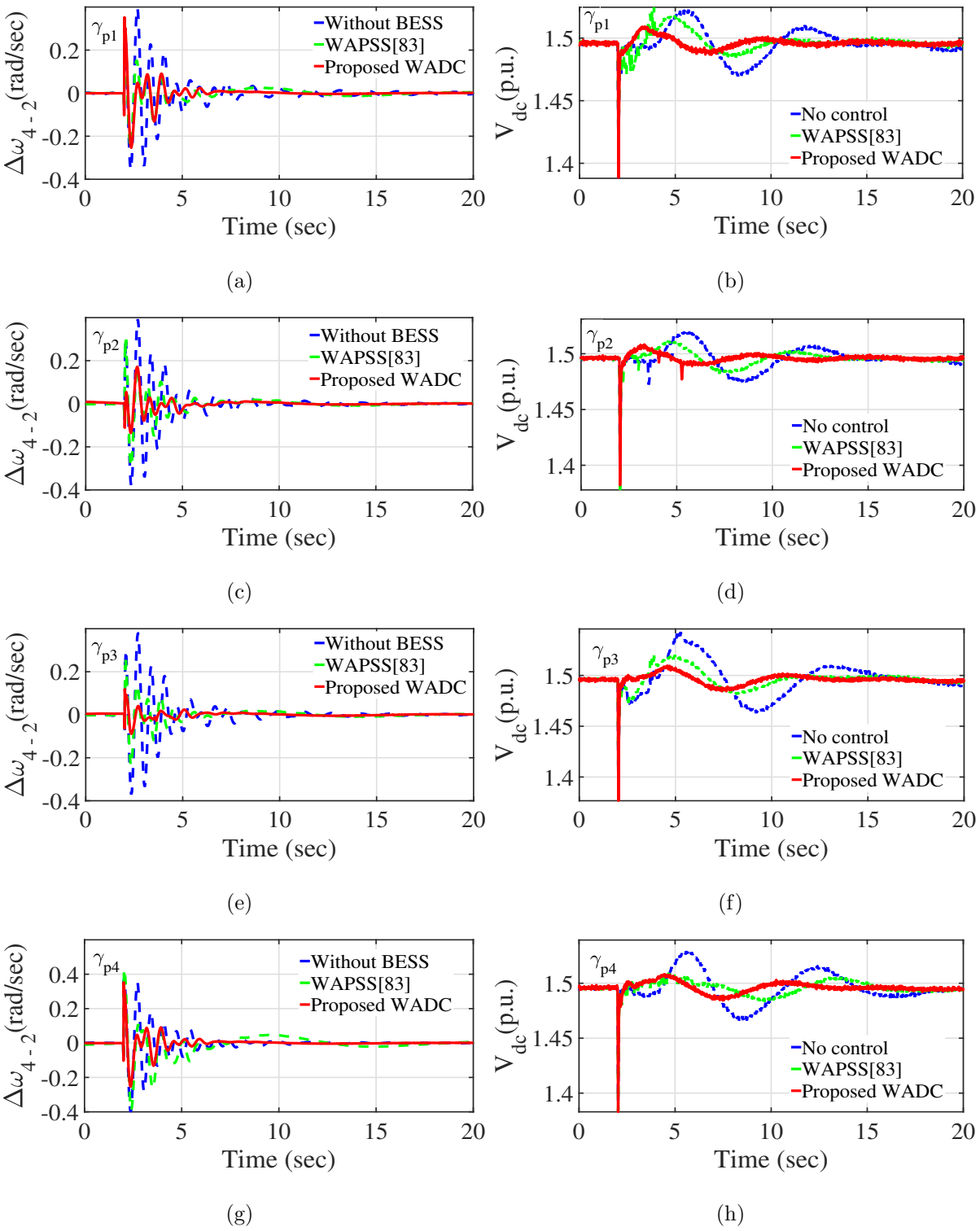

Figure 4.12: Dynamic response of the study system with a WADC for BESS in candidate group ρ_9 under various operating conditions: (a) $\Delta\omega_{4-2}$ under γ_{p1}, (b) V_{dc} under γ_{p1}, (c) $\Delta\omega_{4-2}$ under γ_{p2}, (d) V_{dc} under γ_{p2},(e) $\Delta\omega_{4-2}$ under γ_{p3},(f) V_{dc} under γ_{p3}, (g) $\Delta\omega_{4-2}$ under γ_{p4}, and (h) V_{dc} under γ_{p4}.

BESS under various operating conditions. The proposed WADC for BESS demonstrates superior damping performance compared to the BESS-based WAPSS [83]. However, in candidate group ρ_9, the rotor oscillation and BESS DC link voltage oscillation settling time are slightly increased compared to candidate group ρ_4. Unlike the WADC for BESS in candidate group ρ_9, the proposed WADC for BESS in candidate group ρ_4 effectively damps the prominent inter-area oscillations of the study system under various operating conditions.

4.6.2 Scenario 2 (S2)

In this scenario, the practical study system is simulated with a double line fault applied at t = 3 seconds for a duration of 100 ms on the transmission line between buses 29 and 37. The simulation aims to assess the damping performance of the proposed WADC, which is linked to candidate groups ρ_4 and ρ_9 of the BESS under operating condition γ_{p1}. The dynamic simulation responses, including the rotor speed deviation between SGs 4 and 2, the power flow through line (P_{4-14}), and the BESS active power, are depicted in Fig. 4.13.

From this simulation response, it is revealed that the proposed WADC provided adequate damping to mitigate the SG rotor oscillation, power oscillation in the transmission line, and BESS active power oscillation, performing more effectively compared to the BESS-based WAPSS [83]. The settling time of the rotor oscillation, power oscillation in the transmission line, and BESS active power oscillation in scenario S2 is slightly increased compared to the dynamic simulation response in scenario S1 under operating condition γ_{p1}. The damping performance of the WADC linked with candidate group ρ_4 is better than that with candidate group ρ_9 of the BESS, as shown in Fig. 4.13.

4.6.3 Scenario 3 (S3)

This simulation scenario assesses the robustness of the controller's performance against the variable communication time delay uncertainty in the feedback signal P_{15-14} of the proposed WADC, as shown in Fig. 4.14. This analysis employed variable communication delay range from 100 ms to 300 ms. The practical study system, incorporating the proposed WADC linked with BESS candidate groups ρ_4 and ρ_9, is simulated under operating condition γ_{p1}. During this simulation, a line-to-ground fault is applied to the transmission

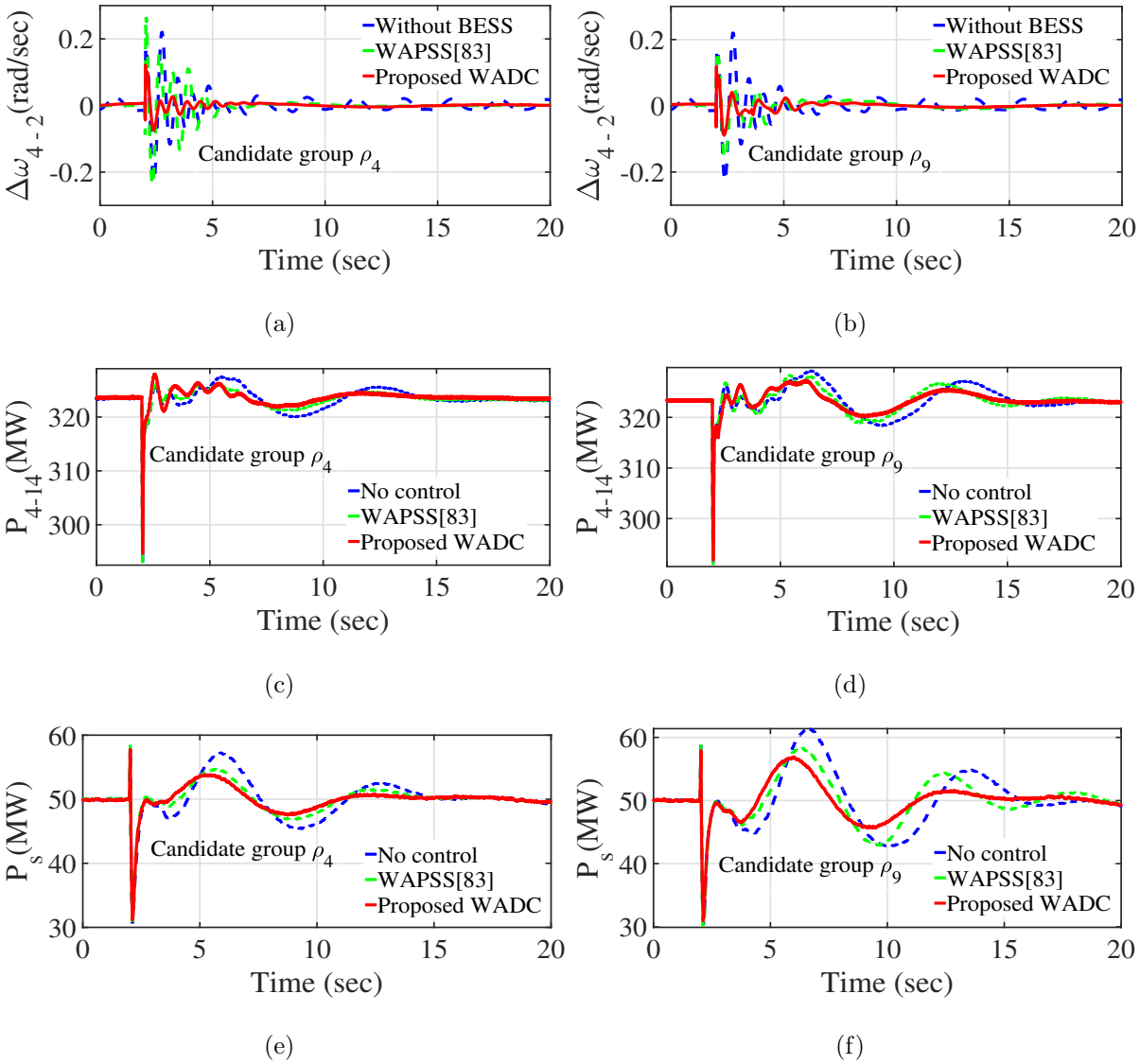

Figure 4.13: Dynamic response of the study system with a WADC for BESS in candidate groups ρ_4 and ρ_9 under operating condition γ_{p1}: (a) $\Delta\omega_{4-2}$ under ρ_4, (b) $\Delta\omega_{4-2}$ under ρ_9, (c) P_{4-14} under ρ_4, (d) P_{4-14} under ρ_9 (e) P_s under ρ_4, and (f) P_s under ρ_9.

line connecting buses 16 and 19, lasting for 100 ms starting at t = 3 sec. The dynamic simulation response encompasses the rotor speed deviation between SG 4 and 2, the power flow through the inter-area line (P_{1-39}), and BESS active power, as depicted in Fig. 4.15.

The results depicted in Fig. 4.15 show that with WADC for BESS in candidate groups ρ_4 and ρ_9, the SG rotor oscillation, power oscillation in the inter-area line, and BESS power oscillation are effectively damped. However, under the system operating condition γ_{p1}, these oscillations have slightly longer settling times than scenarios S1 and S2. The proposed WADC damping performance outperforms the BESS-based WAPSS

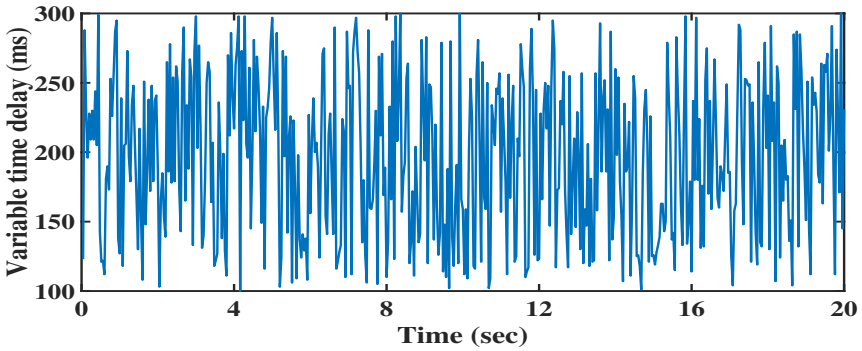

Figure 4.14: Variable communication time delays.

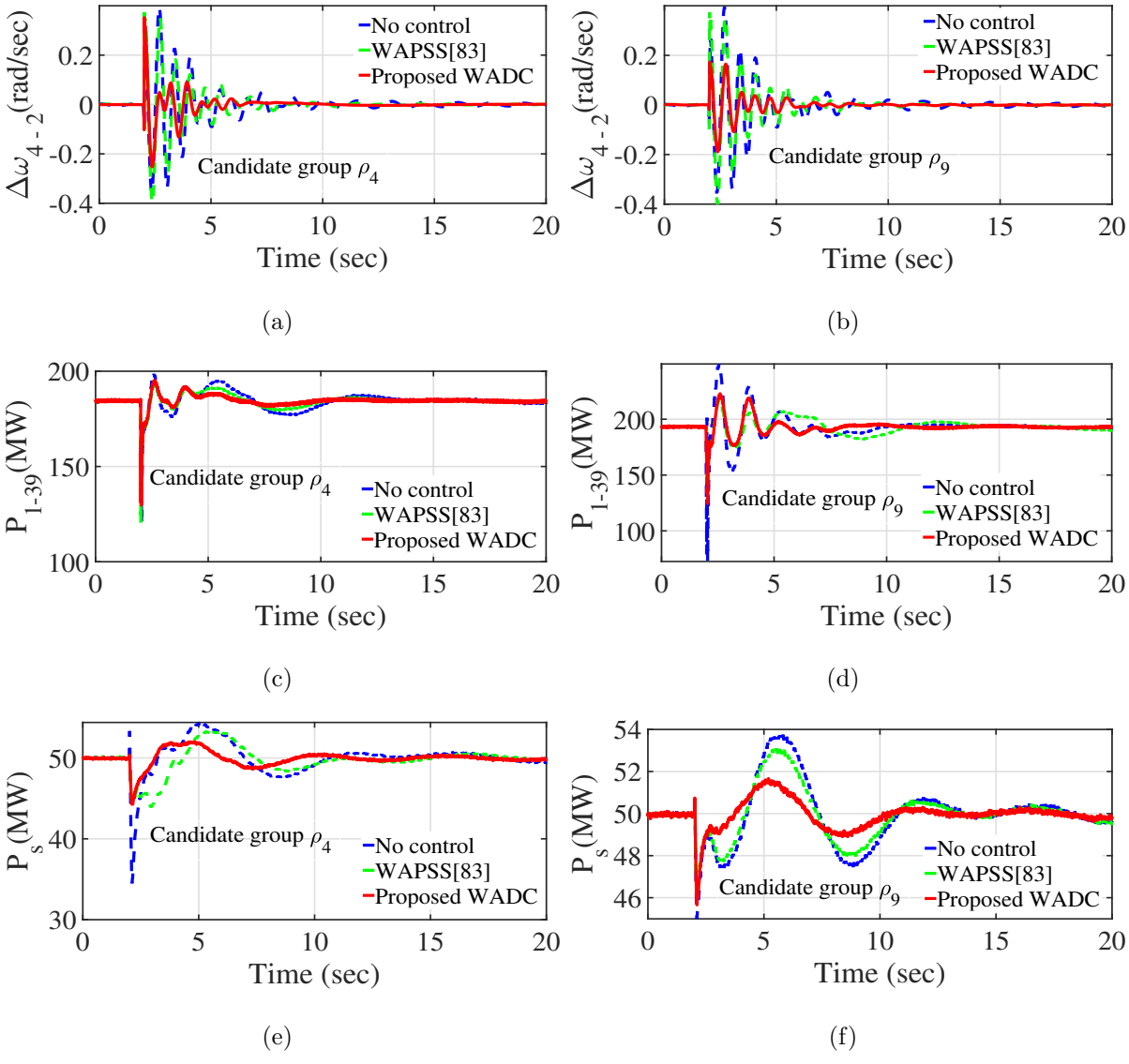

Figure 4.15: Dynamic response of the study system with a WADC for BESS in candidate groups ρ_4 and ρ_9 under operating condition γ_{p1}: (a) $\Delta\omega_{4-2}$ under ρ_4, (b) $\Delta\omega_{4-2}$ under ρ_9, (c) P_{1-39} under ρ_4, (d) P_{1-39} under ρ_9 (e) P_s under ρ_4, and (f) P_s under ρ_9.

[83] regarding variable communication time delay uncertainty.

4.6.4 Scenario 4 (S4)

This scenario integrates a Solar Photovoltaic (PV) system into the modified New England 39-bus system. The solar PV system, with a power capacity of 50 MW, is placed randomly on bus-20 of the study system, as depicted in Fig. 4.16. In this simulation scenario, the solar PV system is configured with 115 solar cells connected in series and 8200 solar cells connected in parallel. Each solar cell operates at its maximum power point condition, generating 17.4 V voltage and 3.05 A current, thus achieving the desired power capacity for the solar PV system. Moreover, under this scenario, the solar PV system is simulated with solar irradiances fixed at 1000 W/m^2 while maintaining a consistent temperature of 25°C throughout the analysis.

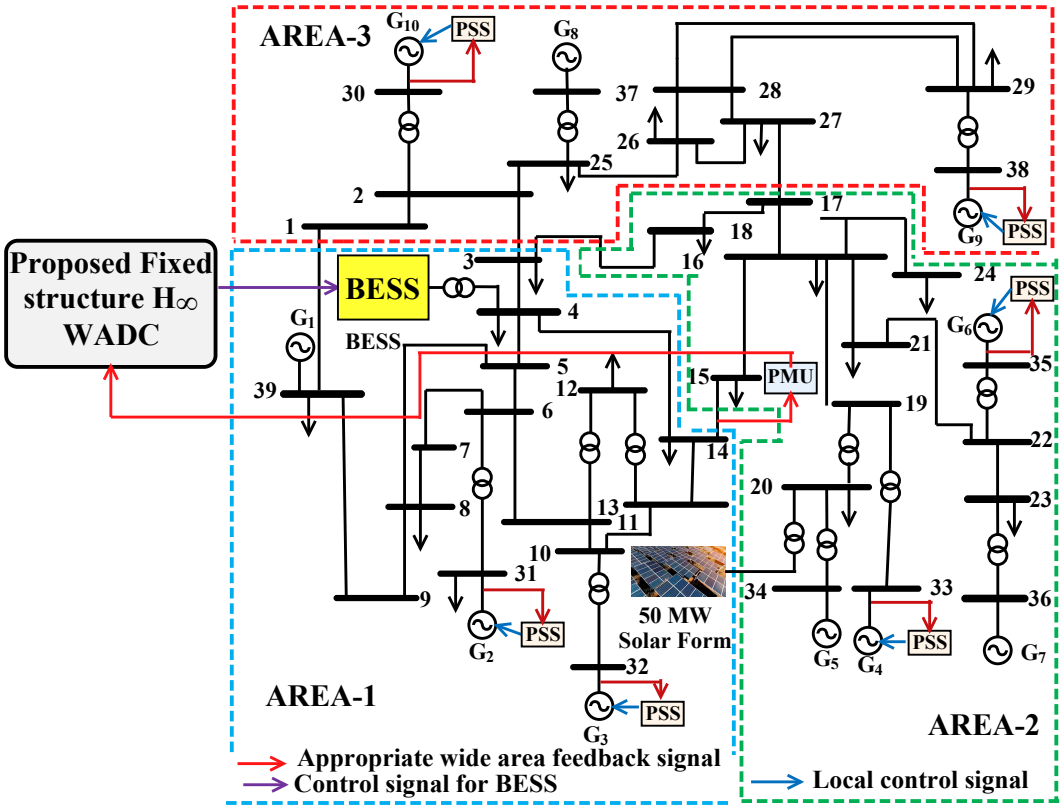

Figure 4.16: Modified New England 39-bus system with WADC for BESS and integrated solar PV system on bus-20.

The dynamic simulation response of rotor speed deviation between SGs 4 and 2 and active power across the inter-are line using WADC for BESS in candidate groups ρ_4 are depicted in Fig. 4.17 (a) and (b), respectively. These dynamic responses reveal that the

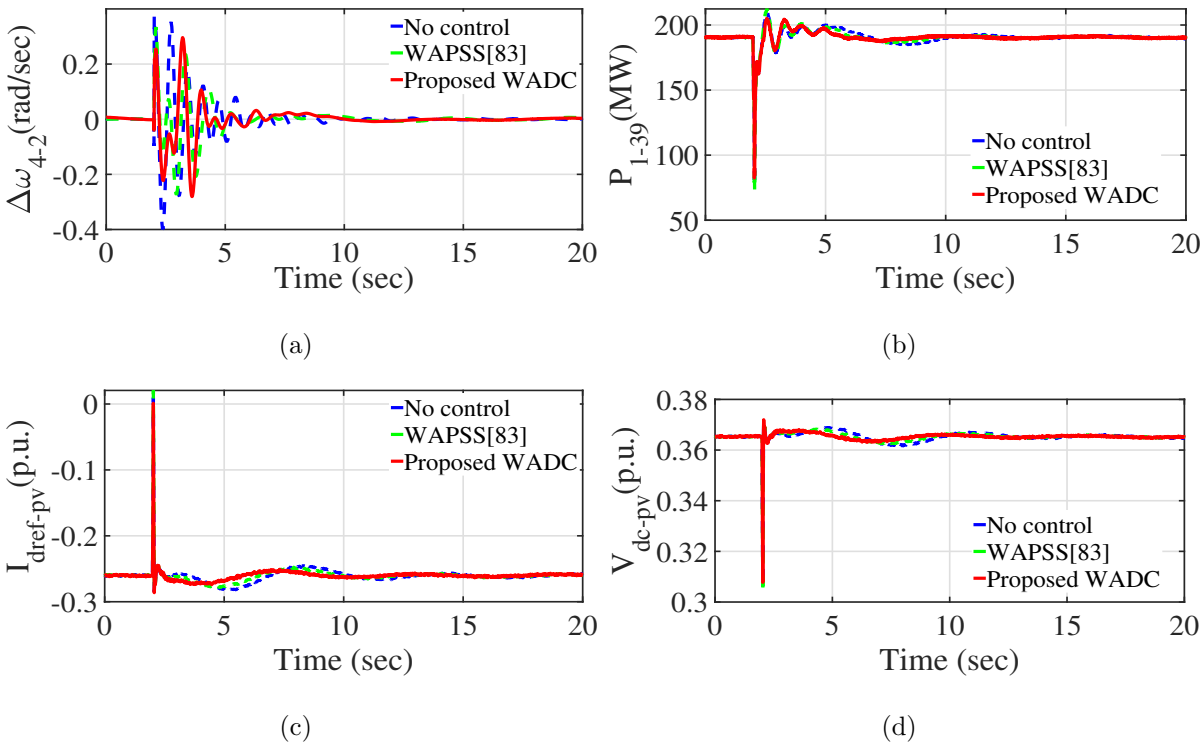

Figure 4.17: Dynamic response of the studied system integrating BESS and a PV system under operating condition γ_{p1} with WADC for BESS in candidate group ρ_4: (a) $\Delta\omega_{4-2}$, (b) P_{1-39}, (c) $I_{dref-PV}$ of GSC in PV system, and (d) V_{dc-PV} of PV system.

proposed WADC provides superior damping performance compared to BESS-based WPSS [83], effectively mitigating the rotor oscillations as well as power oscillation through the inter-area line. The increased settling time of SG rotor oscillations in scenario S4 compared to scenarios S1, S2, and S3 under operating condition γ_{p1}, can be attributed to the lower inertia of converter-based resources compared to conventional generators. Additionally, solar PV systems provide less inherent damping, leading to a sluggish response to disturbances. Consequently, this leads to longer settling times for rotor speed oscillation.

Further dynamic responses of the d-axis reference current of grid-side VSC and DC-link voltage between the boost converter and grid-side converter are depicted in Fig. 4.17 (c) and (d), respectively. These dynamic responses elucidate that the settling time and peak overshoot in the d-axis reference current of the grid-side VSC and the DC-link voltage between the boost converter and the grid-side converter are adequately damped subsequent to a severe contingency in scenario S4. As a result, it is evident that the proposed WADC offers effective damping compared to the WAPSS [83] control scheme in a renewable integration scenario.

The dynamic simulations performed under different scenarios (S1 to S4) confirm the efficacy of the proposed fixed-structure H_∞ WADC for BESS. This control approach demonstrates robust damping performance across various contingencies, encompassing varied system operating conditions, different fault types and locations, uncertainties associated with constant and variable communication time delays in the feedback loop, and integrating renewable sources.

4.6.5 Effect of nonlinearity on proposed WADC for BESS

The proposed WADC for BESS includes nonlinearity, such as actuator saturation of output of the damping controller, as shown in Fig. 4.18. The impact of system damping performance, including nonlinearity on the damping controller, is discussed in [93].

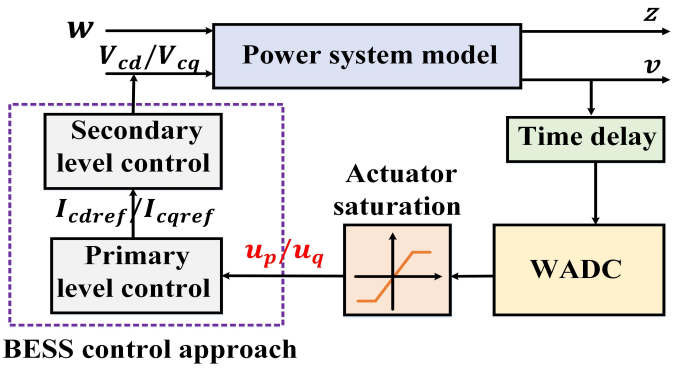

Figure 4.18: WADC with nonlinearity for BESS.

In this simulation case, the actuator saturation limit, characterized by a nonlinear gain function, is applied to the output of the proposed WADC for BESS in candidate group ρ_4 . This saturation limit includes a lower gain of 0.5, an input threshold value of 0.1, and an upper gain of 2. In this case, a three-phase fault is applied on the transmission line between buses 16 and 19 at 3s for 100ms, and the study system is simulated under operating condition γ_{p1}.

The simulation responses of the study system, such as the power flow through inter-area line P_{1-39}, the active power of the BESS, the DC link voltage between the DC-DC bidirectional converter and the VSC of the BESS, and the d-axis reference current for the VSC of the BESS, are shown in Fig. 4.19 (a), (b), (c), and (d), respectively. These results demonstrate that the oscillations occurring after a severe disturbance in the system are reduced compared to the WAPSS suggested in [83]. Additionally, the simulation response

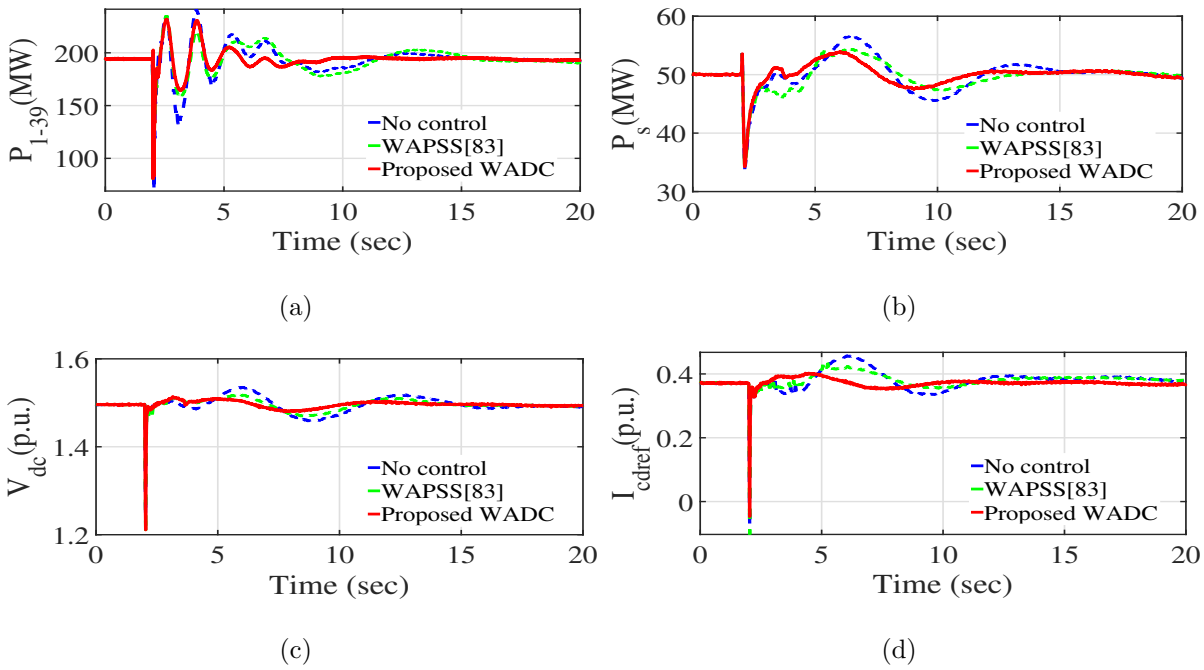

Figure 4.19: Dynamic response of the study system with a WADC linked with nonlinearity for BESS in candidate ρ_4 under operating condition γ_{p1}: (a) P_{1-39} (b) P_s, (c) V_{dc}, and (d) I_{cdref}.

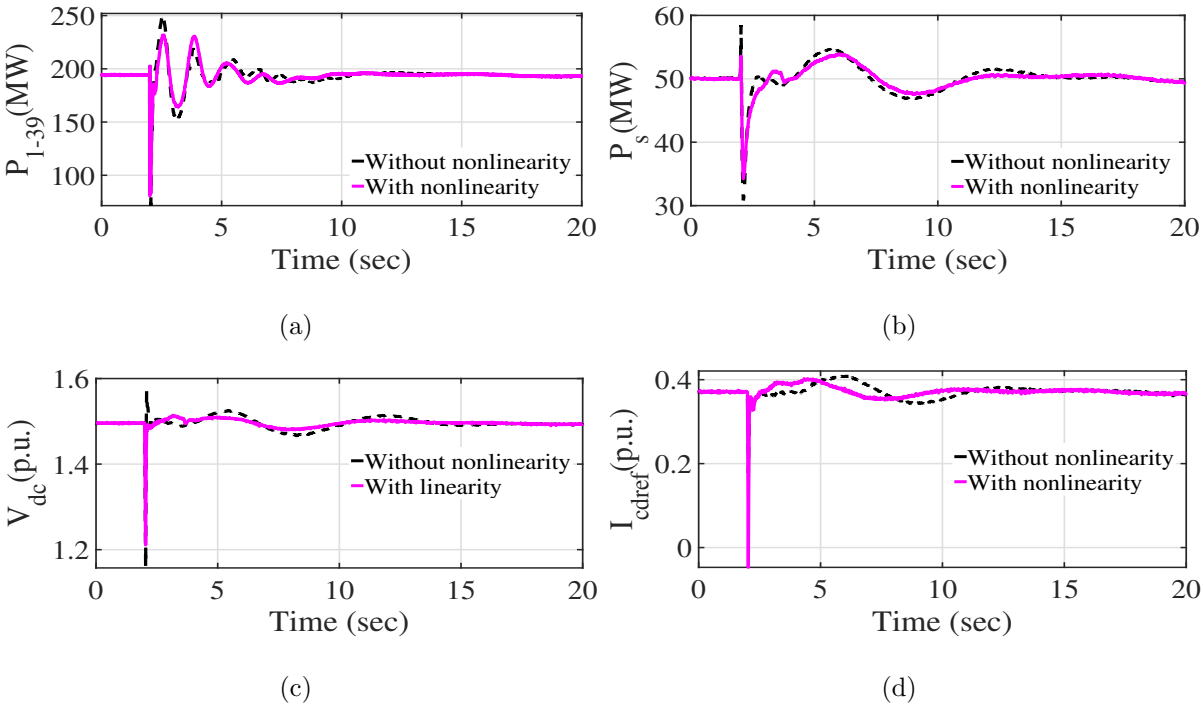

Figure 4.20: Dynamic response of the study system with a WADC linked without and with nonlinearity for BESS in candidate ρ_4 under operating condition γ_{p1}: (a) P_{1-39} (b) P_s, (c) V_{dc}, and (d) I_{cdref}.

of the study system with the proposed WADC for the BESS, including with and without nonlinearity, is depicted in Fig. 4.20. From this simulation response, it is observed that the WADC with nonlinearity effectively reduces the peak amplitude of oscillations in the inter-area line power flow, the output power of the BESS, the DC link voltage of the VSC of the BESS, and the VSC current of the BESS, providing superior damping performance compared to the WADC without nonlinearity. Consequently, the presence of nonlinearity in the damping controller notably reduces the system's oscillation response, enhances its overall damping performance, and prevents excessive control actions during severe disturbances.

4.7 Summary

In this study, a fixed-structure H_∞ scheme-based WADC is designed for the BESS integrated power system. The location for installing BESS and the appropriate damping control loops, such as feedback signal and control loop (i.e., an active or reactive loop of BESS) to link the damping controller, are identified using the maximal of all minimal residues indices under various operating conditions of the system. This study unveils that the BESS active power control loop exhibits superior damping performance compared to the reactive power control loop in mitigating dominant inter-area oscillations under varying system operating conditions. The superiority of the proposed controller is confirmed by comparing the proposed WADC with the fixed-structure H_∞ WADC placed in the reactive power control loop, as well as a BESS-based WAPSS linked into active and reactive power control loops. The proposed fixed-structure H_∞ WADC is implemented in RTDS to assess its viability in a real-time environment. The outcomes of dynamic simulation and small-signal analysis validate the effectiveness of the proposed WADC in a multi-machine power system and are found to be superior.